Journal of Computational Physics **153,** 353–377 (1999)
Article ID jcph.1999.6281, available online at http://www.idealibrary.com on IDEAL®

Diffusion Characteristics of Finite Volume and Fluctuation Splitting Schemes

William A. Wood* and William L. Kleb†

NASA Langley Research Center, Hampton, Virginia 23681
E-mail: *w.a.wood@larc.nasa.gov; †w.l.kleb@larc.nasa.gov

Received November 13, 1998; revised March 29, 1999

The diffusive characteristics of two upwind schemes, multi-dimensional fluctuation splitting and locally one-dimensional finite volume, are compared for scalar advection–diffusion problems. Algorithms for the two schemes are developed for node-based data representation on median-dual meshes associated with unstructured triangulations in two spatial dimensions. Four model equations are considered: linear advection, non-linear advection, diffusion, and advection–diffusion, with cases chosen to mimic features present in compressible gas dynamics. Modular coding is employed to isolate the effects of the two approaches for upwind flux evaluation, allowing for head-to-head accuracy and efficiency comparisons. Both the stability of compressive limiters and the amount of artificial diffusion generated by the schemes are found to be grid-orientation dependent, with the fluctuation splitting scheme producing less artificial diffusion than the finite volume scheme. Convergence rates are compared for an advection–diffusion problem, with a speedup of 2.5 seen for fluctuation splitting versus finite volume when solved on the same mesh. However, accurate solutions to problems with small diffusion coefficients can be achieved on coarser meshes using fluctuation splitting rather than finite volume, so that when comparing convergence rates to reach a given accuracy, fluctuation splitting shows a speedup of 29 over finite volume for the test problem.

Key Words: finite volume; fluctuation splitting; artificial dissipation.

INTRODUCTION

Upwind discretizations for advection equations typically introduce artificial numerical dissipation into the solution. When combined advection–diffusion problems are considered, this dissipation introduced in the discretization of the advection terms should be less than the true physical diffusion. Here, the diffusive charactersitics of upwind advection schemes are investigated on unstructured triangulations, and their performance in resolving solutions to combined advection–diffusion problems, with small diffusion coefficients, is quantitatively assessed.

0021-9991/99 $30.00

Two node-based, median-dual methods for modeling convective fluxes are considered. The first is a traditional locally one-dimensional approximate Riemann solver finite volume (FV) scheme [1]. Locally one-dimensional schemes applied on multidimensional domains are known to introduce excess dissipation when discontinuities are not aligned with the mesh [2].

The second method is the narrow non-linear [3] fluctuation splitting (FS) scheme, also referred to in the literature as a residual distribution scheme. FS has a more compact stencil than FV for second-order formulations and exhibits zero cross diffusion in a grid-aligned condition. Both of these attributes should lead to less artificial dissipation as compared with FV.

The sensitivity of FS and FV to grid orientation and resulting production of cross diffusion is investigated in the present report. The use of compressive limiter functions is also tested with both algorithms. Local timesteps based on positivity arguments are implemented for both first- and second-order discretizations of the implicit matrix.

Formulation of FS schemes for diffusion problems is a recent research area [4, 5]. The present study seeks to quantify the relative merits of using a low-diffusion advection operator to resolve advection–diffusion problems with small diffusion coefficients. Lessons learned on these problems will guide the development of computer codes for solving compressible viscous fluid dynamic problems. A similar approach for central difference schemes with explicit numerical dissipation has recently been taken by Efraimsson [6].

The model problems considered are linear advection, non-linear advection, linear diffusion, and linear advection–diffusion. These problems are intended to mimic behavior expected from applications to gas dynamics such as supersonic, inviscid, perfect-gas flow (non-linear advection), and high-Reynolds-number shear flows (advection–diffusion).

GOVERNING EQUATIONS

The non-linear advection–diffusion equation,

$$u_t + \nabla \cdot \vec{F} = \nabla \cdot (\nu \nabla u), \tag{1}$$

is cast as a hyperbolic conservation law, to which steady-state solutions are sought. Here u is the dependent variable, $\vec{F} = \vec{F}(x, y, u)$ is the convective flux function, and ν is the diffusion coefficient.

Finite Volume

In FV form, using the divergence theorem Eq. (1) becomes

$$\int_\Omega u_t \, d\Omega = -\oint_\Gamma (\vec{F} - \nu \nabla u) \cdot \hat{n} \, d\Gamma, \tag{2}$$

where Ω is the median dual about node i, Γ is the boundary of Ω, and $\hat{n}$ is the outward unit normal to control cell. Using mass lumping to the nodes, similar to an explicit finite element treatment [7], the temporal evolution is evaluated on a time-invariant mesh as

$$\int_\Omega u_t \, d\Omega = S_i \frac{\partial u_i}{\partial t} \rightarrow \frac{S_i}{\tau}\left(u_i^{t+\tau} - u_i^t\right), \tag{3}$$

where S_i is the median-dual area about node i and τ is the time step.

The discretization of the convective flux, $\vec{F}$, is constructed following Barth's [1] implementation of the upwind, locally one-dimensional, approximate Riemann solver of Roe [8],

$$\oint_\Gamma \vec{F}\cdot\hat{n}\,d\Gamma \to \sum_{\text{faces}}\left[\frac{1}{2}(\vec{F}_{\text{in}}+\vec{F}_{\text{out}})\cdot\hat{n}-\Phi\right]\Delta\Gamma, \tag{4}$$

where the artificial dissipation, Φ, provides the upwinding,

$$\Phi=\frac{1}{2}|\tilde{A}\hat{n}_x+\tilde{B}\hat{n}_y|(u_{\text{out}}-u_{\text{in}}), \tag{5}$$

with $\hat{n}=\hat{n}_x\hat{\imath}+\hat{n}_y\hat{\jmath}$ ($\hat{\imath}$ and $\hat{\jmath}$ are the Cartesian unit vectors). "Out" and "in" refer to states on the outside and inside of Ω at the face. A and B are the flux Jacobians in the $\hat{\imath}$ and $\hat{\jmath}$ directions, respectively,

$$A=\frac{\partial F^{(1)}}{\partial u},\qquad B=\frac{\partial F^{(2)}}{\partial u}, \tag{6}$$

and ($\tilde{A}$, $\tilde{B}$) represent their conservative linearizations at the cell face [8].

Piecewise linear reconstruction from the nodal unknowns to the cell faces as

$$u_{\text{face}}=u_i+\psi\nabla u\cdot\vec{r} \tag{7}$$

provides second-order spatial accuracy in smoothly varying regions of the solution. $\vec{r}$ is the position vector from the node to the face. Median-dual gradients of the dependent variable, ∇u, are obtained from the unweighted least squares procedure outlined by Barth. Following Bruner and Walters [9], the limiter function, ψ, is supplied an argument equal to half the argument Barth uses, namely,

$$\psi=\psi\left(\frac{u^{\min/\max}-u_i}{2(\nabla u\cdot\vec{r})^{\min/\max}}\right), \tag{8}$$

where $u^{\min/\max}$ is the minimum (resp. maximum) of u_i and all distance-one neighbors. The more restrictive constraint from using either the maximum or minimum is used to set the limiter value.

In casting the limiter argument in this form, Bruner equates the Barth limiter with Superbee, for a limiter argument less than or equal to one. The Barth limiting is non-symmetric, taking the form

$$\psi\left(\frac{p}{q}\right)=\begin{cases}0 & \frac{p}{q}\le 0\\ 2\frac{p}{q} & \text{if } 0<\frac{p}{q}<\frac{1}{2}\\ 1 & \frac{p}{q}\ge\frac{1}{2}\end{cases} \tag{9}$$

for the limiter as cast in Eq. (8). In Eq. (9), p and q are dummy arguments for the limiter.

Two methods for evaluating the physical diffusion term are incorporated into FV. The more compact of the two, the finite element discretization, is discussed in the following

section. The less compact diffusion formula is obtained by discretizing the last term of Eq. (2), in a manner similar to Eq. (4),

$$\oint_{\Gamma} \nu \nabla u \cdot \hat{n}\, d\Gamma \rightarrow \sum_{\text{faces}} \frac{\overline{\nu}}{2} (\nabla u_{\text{in}} + \nabla u_{\text{out}}) \cdot \hat{n} \Delta\Gamma. \tag{10}$$

The diffusion coefficient is averaged over the length of the face. The gradients from Eq. (7) are not limited before averaging at the control-volume faces in Eq. (10). Discretizing the diffusion terms in this manner would lead to a five-point stencil on a one-dimensional structured mesh.

Fluctuation Splitting

The NNL FS scheme is presented as a slight rederivation of the work of Sidilkover and Roe [3]. The current interpretation is as a volume integral over triangular elements, without recourse to the divergence theorem. The discretized equations, however, are identical.

Integrating Eq. (1) over an element, where Ω is now the area of the triangular element,

$$\int_{\Omega} u_t\, d\Omega = -\int_{\Omega} \nabla \cdot \vec{F}\, d\Omega + \int_{\Omega} \nabla \cdot (\nu \nabla u)\, d\Omega. \tag{11}$$

For linear variation of the dependent variable over the element, the temporal evolution is

$$\int_{\Omega} u_t\, d\Omega = \Omega \overline{u}_t = \frac{\Omega}{3} \left(u_{1_t} + u_{2_t} + u_{3_t} \right), \tag{12}$$

where u_1, u_2, and u_3 correspond to the three nodes defining element Ω.

Defining local curvilinear coordinates, ξ and η, parallel to sides $\overline{12}$ and $\overline{23}$, respectively (Fig. 1), the divergence of the convective flux can be written

$$\nabla \cdot \vec{F} = F_x^{(1)} + F_y^{(2)} = \frac{1}{J^{-1}} (\hat{n}_2 \cdot \vec{F}_{\xi} - \hat{n}_1 \cdot \vec{F}_{\eta}), \tag{13}$$

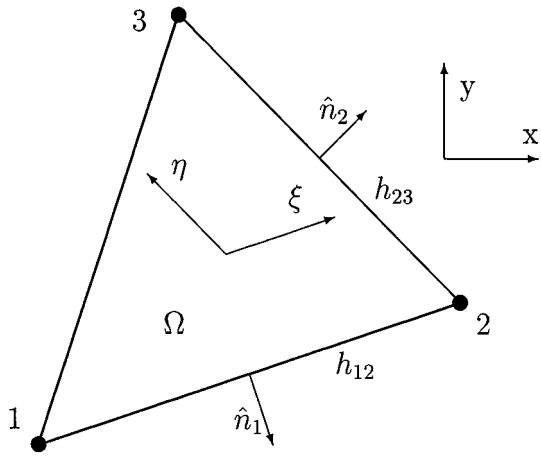

FIG. 1. Fluctuation splitting element nomenclature.

where J^{-1} is the inverse Jacobian of the coordinate transformation. Defining the scaled inward normal, $\mathbf{n} = -h\hat{n}$, where h is a mesh edge length, the divergence (Eq. (13)) becomes

$$\nabla \cdot \vec{F} = \frac{1}{2\Omega}(-h_{12}\mathbf{n}_2 \cdot \vec{F}_\xi + h_{23}\mathbf{n}_1 \cdot \vec{F}_\eta). \tag{14}$$

A feature of Sidilkover's scheme is that the choice is arbitrary for which two of the three sides of the triangle to use for ξ and η, provided they follow a right-hand rule for axes. Most other FS implementations [10–12] require the identification of inflow and outflow edges to set the local coordinates for each cell. Preliminary numerical tests during the present study varied the choice of sides for (ξ, η), and while the transient behavior differed, the converged steady-state solutions were identical. For all results presented here the choice for the (ξ, η) vertex is chosen arbitrarily to be the second node of the triangle as defined by the grid generator.

If $\vec{F}$ is linear or quadratic in u, then for a linear variation of u over the element,

$$\int_\Omega \nabla \cdot \vec{F}\, d\Omega = \alpha \Delta_{21} u + \beta \Delta_{32} u, \tag{15}$$

where the difference operator is defined as $\Delta_{21} u = u_2 - u_1$, and the advection speeds are

$$\alpha = -\frac{1}{2}\left(\mathbf{n}_{2_x}\tilde{A} + \mathbf{n}_{2_y}\tilde{B}\right), \qquad \beta = \frac{1}{2}\left(\mathbf{n}_{1_x}\tilde{A} + \mathbf{n}_{1_y}\tilde{B}\right), \tag{16}$$

where $\tilde{A}$ and $\tilde{B}$ are now conservative linearizations over the triangular element [13].

The advective fluctuation, ϕ, is defined as

$$\phi = -\int_\Omega \nabla \cdot \vec{F}\, d\Omega. \tag{17}$$

The fluctuation is split according to

$$\phi = \phi^\xi + \phi^\eta, \tag{18}$$

where

$$\phi^\xi = -\alpha \Delta_{21} u, \qquad \phi^\eta = -\beta \Delta_{32} u. \tag{19}$$

Following Sidilkover [14] the fluctuation is limited to achieve a second-order scheme. The limited fluctuations are given by

$$\phi^{\xi^*} = \phi^\xi + \phi^\eta \psi(Q) = \phi^\xi \left(1 - \frac{\psi(Q)}{Q}\right), \qquad \phi^{\eta^*} = \phi^\eta - \phi^\eta \psi(Q) = \phi^\eta (1 - \psi(Q)), \tag{20}$$

with

$$Q = -\frac{\phi^\xi}{\phi^\eta}. \tag{21}$$

Upwinding is achieved through the introduction of artificial dissipation terms,

$$\bar{\phi}^\xi = \text{sign}(\alpha)\phi^{\xi^*}, \qquad \bar{\phi}^\eta = \text{sign}(\beta)\phi^{\eta^*}. \tag{22}$$

Combining Eq. (12) with a distribution scheme for Eq. (17) and summing over all elements, the contributions to nodal time derivatives can be written in the form

$$\begin{aligned} S_1 u_{1_t} &\leftarrow \frac{1}{2}(\phi^{\xi^*} - \bar{\phi}^{\xi}) + \text{COE} \\ S_2 u_{2_t} &\leftarrow \frac{1}{2}(\phi^{\xi^*} + \bar{\phi}^{\xi}) + \frac{1}{2}(\phi^{\eta^*} - \bar{\phi}^{\eta}) + \text{COE} \\ S_3 u_{3_t} &\leftarrow \frac{1}{2}(\phi^{\eta^*} + \bar{\phi}^{\eta}) + \text{COE}, \end{aligned} \tag{23}$$

where COE stands for contributions from other elements containing these nodes. The nodal distribution formula can also be written in a compact form,

$$S_i u_{i_t} \leftarrow \frac{1}{4}[i(3-i)(\phi^{\xi^*} + (-1)^i \bar{\phi}^{\xi}) + (-4 + 5i - i^2)(\phi^{\eta^*} - (-1)^i \bar{\phi}^{\eta})] + \text{COE}. \tag{24}$$

A finite element treatment, similar to that of Tomaich [4], is employed to obtain the diffusive fluctuation, ϕ_v, as

$$\phi_v = \int_\Omega \nabla \cdot (\nu \nabla u)\, d\Omega. \tag{25}$$

Assuming piecewise-linear data and an element-averaged diffusion coefficient leads to a diffusive fluctuation of zero for the triangular element. Introducing the linear nodal shape functions ϑ_i, such that $\sum_{i=1}^{3} \vartheta_i = 1$, the elemental diffusive fluctuation can be expressed $\phi_v = \sum_{i=1}^{3} \phi_{v_i} = 0$, where

$$\phi_{v_i} = \int_\Omega \vartheta_i \nabla \cdot (\nu \nabla u)\, d\Omega. \tag{26}$$

Integrating by parts,

$$\phi_{v_i} = \oint_\Gamma \vartheta_i \nu \nabla u \cdot \hat{n}\, d\Gamma - \int_\Omega \nu \nabla u \cdot \nabla \vartheta_i\, d\Omega. \tag{27}$$

The boundary integral in Eq. (27) will cancel upon summing contributions for interior nodes. The remaining volume integral can be evaluated analytically,

$$\phi_{v_i} = -\frac{\bar{\nu}}{2} \nabla u \cdot \mathbf{n}_{i+1} = -\frac{\bar{\nu}}{4\Omega} \sum_{j=1}^{3} u_j \mathbf{n}_{j+1} \cdot \mathbf{n}_{i+1}. \tag{28}$$

Distributing this diffusive fluctuation to the nodes and keeping only the larger of the physical or artificial dissipation leads to the update formula,

$$\begin{aligned} S_1 u_{1_t} &\leftarrow \frac{\phi^{\xi^*}}{2} + \max\left(-\frac{\bar{\phi}^{\xi}}{2}, \phi_{v_1}\right) + \text{COE} \\ S_2 u_{2_t} &\leftarrow \frac{\phi^{\xi^*} + \phi^{\eta^*}}{2} + \max\left(\frac{(\bar{\phi}^{\xi} - \bar{\phi}^{\eta})}{2}, \phi_{v_2}\right) + \text{COE} \\ S_3 u_{3_t} &\leftarrow \frac{\phi^{\eta^*}}{2} + \max\left(\frac{\bar{\phi}^{\eta}}{2}, \phi_{v_3}\right) + \text{COE}. \end{aligned} \tag{29}$$

BOUNDARY CONDITIONS

Explicit Dirichlet inflow boundary conditions are employed. Advective outflow boundaries are treated for free convection through the boundary nodes, allowing boundary nodes to be handled in the same manner as interior nodes. For the diffusion terms a Neumann outflow boundary is applied with zero gradient, achieved by setting the boundary integral in Eq. (27) to zero.

LIMITER FUNCTIONS

Minmod, van Albada [15], Superbee, and γ [16] symmetric limiters are utilized for FV (Eq. (7)) and FS (Eq. (20)) in the form of symmetric averaging functions, M, related to the limiter as

$$q\psi\left(\frac{p}{q}\right) = M(p,q) = M(q,p) = p\psi\left(\frac{q}{p}\right).$$

The van Albada averaging function is

$$M = \frac{(pq+\varepsilon^2)(p+q)}{p^2+q^2+2\varepsilon^2},$$

where the small parameter ε^2 varies like Δx^3 (see [15, 17] for discussion on scaling ε) and serves to reduce the limiting in smooth regions.

The averaging function for the γ limiter, of which the Minmod ($\gamma = 1$) and Superbee ($\gamma = 2$) are special cases, is

$$M(p,q) = \begin{cases} 0 & pq \le 0 \\ \gamma p & \gamma|p| \le |q| \\ q & \text{if } |p| \le |q| \le \gamma|p|. \\ p & |q| \le |p| \le \gamma|q| \\ \gamma q & \gamma|q| \le |p| \end{cases} \tag{30}$$

TIMESTEP

Both schemes are formulated as Gauss–Seidel time-relaxation algorithms. The nodal updates for the discrete system can be formed as a sum of contributions from all nodes:

$$u_i^{t+\tau} = \sum_j c_j u_j = c_i u_i + \sum_{j\neq i} c_j u_j. \tag{31}$$

For positivity [18] each of the coefficients, c_j, in Eq. (31) must be non-negative.

Advective Timestep Restriction

In the FV context the nodal update (Eq. (31)) can be rearranged into the form of Eq. (3),

$$\frac{S_i}{\tau}\left(u_i^{t+\tau} - u_i^t\right) = \frac{S_i}{\tau}(c_i - 1)u_i + \frac{S_i}{\tau}\sum_{j\neq i} c_j u_j. \tag{32}$$

For the upwind, edge-based algorithm considered here, each $(S_i/\tau)c_j$ will be related to a positive-definite coefficient equal to zero for outflowing faces and related to the wavespeed for inflowing faces, yielding the restriction $\tau \geq 0$ on the timestep. The remaining term can be expressed as

$$\frac{S_i}{\tau}(c_i - 1) = -\sum_{k \text{ about } i} c_k, \tag{33}$$

where the c_k coefficients, k in this case referring to nodes neighbor-1 with node i, are also positive-definite, either zero for inflowing faces or related to the wavespeed for outflowing faces. Rearranging and imposing the positivity constraint, $c_i \geq 0$, yields the timestep restriction

$$1 - \frac{\tau}{S_i}\sum_{k \text{ about } i} c_k = c_i \geq 0. \tag{34}$$

The timestep is then obtained,

$$\tau \leq \frac{S_i}{\sum_{k \text{ about } i} c_k}. \tag{35}$$

For FS, the nodal updates are assembled from Eq. (23) as

$$\frac{S_i}{\tau}\left(u_i^{t+\tau} - u_i^t\right) = \sum_{j \neq i} c_j (u_j - u_i). \tag{36}$$

In this case the c_j coefficients are formed as contributions from the fluctuations in the triangles to both the left and the right of mesh edge $\overline{IJ}$. The positivity restriction on τ is found to have a similar form as for finite volume (Eq. (35)),

$$\tau \leq \frac{S_i}{\sum_{j \neq i} c_j}. \tag{37}$$

Local timestepping based on positivity is shown to yield stable, yet non-converging, solutions in some second-order cases (see Results). Robust convergence is obtained by using the first-order c's in Eq. (35) and (37), even with second-order-accurate spatial discretizations. This is analogous to the common practice in the FV community of using a first-order left-hand-side Jacobian discretization in an implicit scheme.

Diffusive Timestep Restriction

Unfortunately, the finite element formulation for the diffusive terms (Eq. (28)) cannot be guaranteed to preserve local positivity on obtuse triangles (see Barth [1]). Considering only the contributions from the current node, the coefficient for the diffusion term can be written as

$$u_i^{t+\tau} = u_i^t\left(1 - \frac{\tau}{S_i}\sum_T \frac{\nu \ell^2}{4\Omega}\right), \tag{38}$$

where the appropriate edge length, ℓ, is the side of the element opposite the current node. The resulting timestep restriction is,

$$\tau \leq \frac{S_i}{\sum_T \nu \ell^2/4\Omega}. \tag{39}$$

In a similar manner the timestep restriction for Eq. (10) is

$$\tau \leq \frac{S_i}{\sum_T 3\nu\Delta\Gamma^2/4\Omega}. \tag{40}$$

RESULTS

Linear Advection

The linear advection equation is obtained from Eq. (1) by setting $\nu = 0$ and $\vec{F} = \vec{\lambda}u$, yielding

$$u_t + \nabla \cdot (\vec{\lambda}u) = 0. \tag{41}$$

An analytically non-divergent advection velocity is considered, such that $\nabla \cdot \vec{\lambda} = 0$. Equation (41) can then be written

$$u_t + \vec{\lambda} \cdot \nabla u = 0. \tag{42}$$

Uniform advection. Uniform advection of the Heaviside function at -45°, $\vec{\lambda} = (1, -1)$, on a cut-Cartesian mesh is shown for second-order FS and FV in Figs. 2 and 3, respectively. The mesh is shown as the dashed background, and equally spaced contours vary on [0, 1], the minimum and maximum solution values. The spread of the contour lines with spatial evolution is indicative of the amount of dissipation introduced into the solution by the discretization of the convective terms. FS represents a significant reduction in numerical diffusion versus the corresponding FV scheme, with both results employing the Minmod limiter.

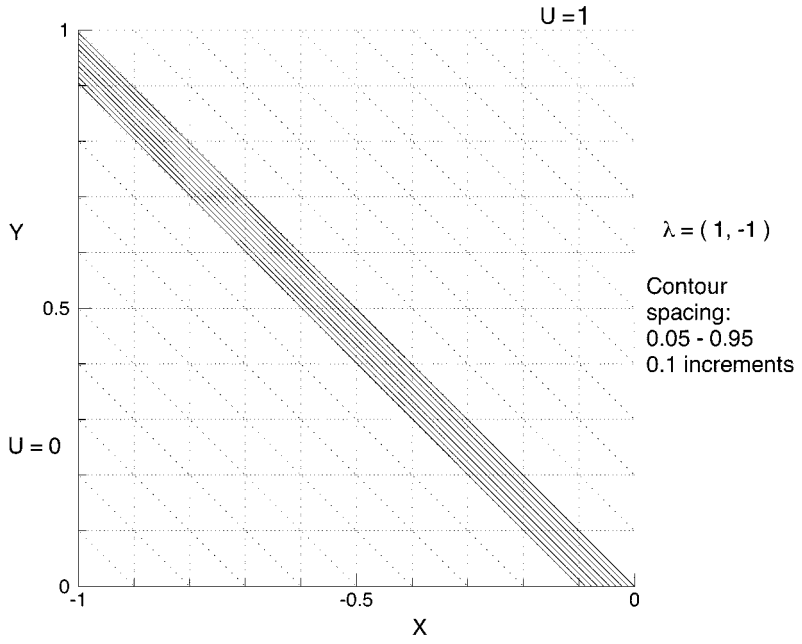

FIG. 2. Second-order fluctuation splitting, uniform advection.

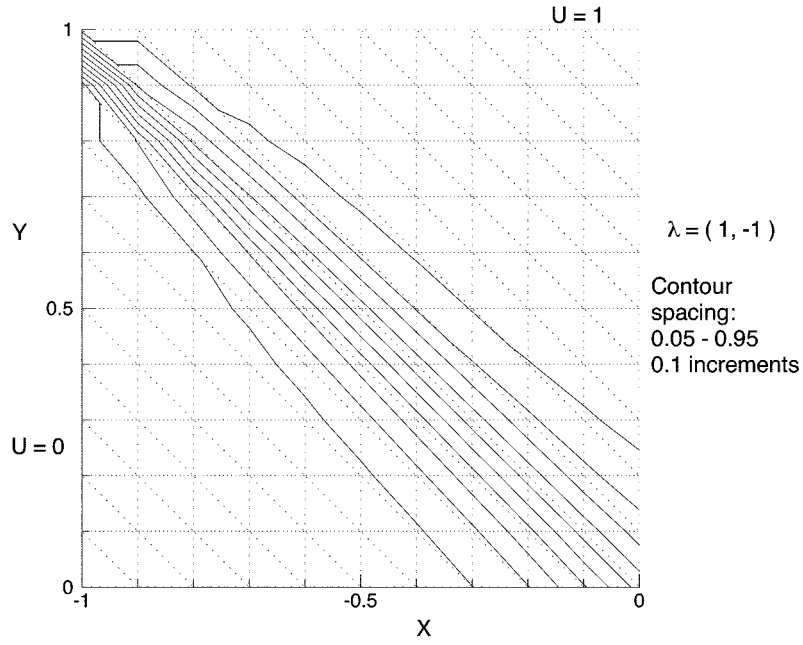

FIG. 3. Second-order finite volume, uniform advection.

However, the "zero cross diffusion" results of Fig. 2 with FS are misleading. In Fig. 4 the advection velocity has been rotated counterclockwise by 90° on the same grid. Clearly, the artificial dissipation introduced by the FS scheme has been increased. The corresponding FV solution, not shown (see [19]), also has an increase in artificial dissipation production versus the favorably aligned mesh of Fig. 3.

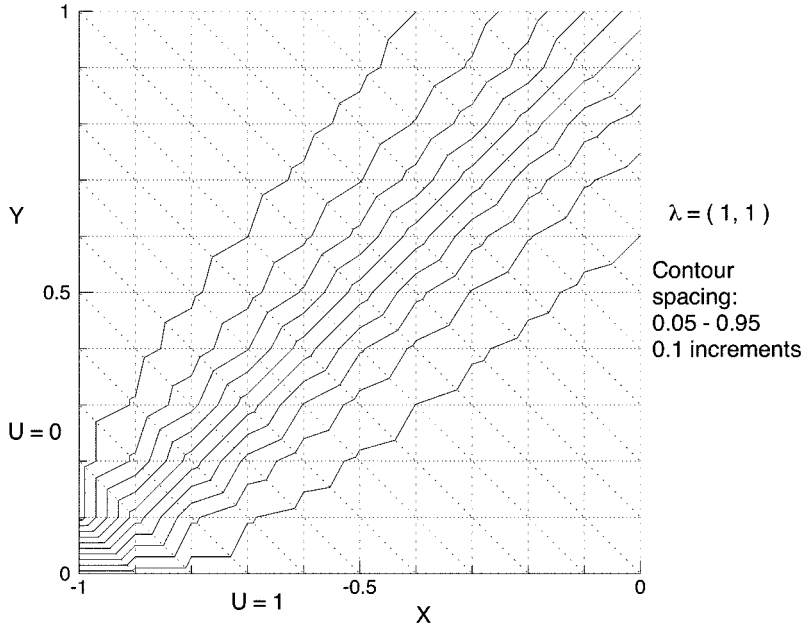

FIG. 4. Second-order fluctuation splitting, uniform advection.

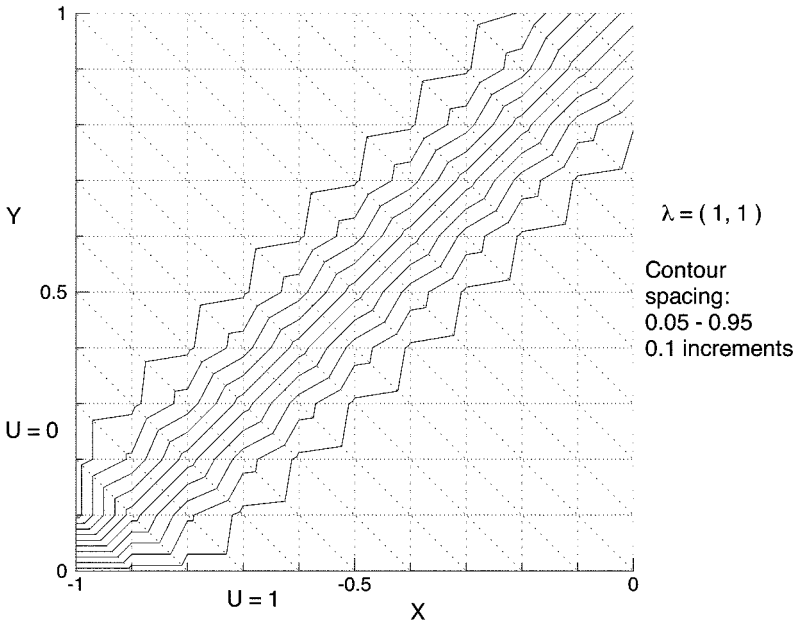

FIG. 5. Second-order fluctuation splitting with compressive limiter.

Employing the compressive Superbee limiter with the FS scheme yields the results shown in Fig. 5. In this case the discontinuity is confined to a 2–3 cell stencil and does not grow in space. Applying the Superbee limiter to FV cannot eliminate all artificial dissipation for this case, as is possible with FS. The FV results, not shown (see [19]), corresponding to the FS results of Fig. 5 show a continual broadening of the discontinuity, eventually reaching a width of four cells by the outflow boundary.

However, while it is possible to use the Superbee limiter with FS for this case, compressive limiters can be unstable for certain grid orientations. For example, no degree of compression is stable for the case of Fig. 2. This instability is due to a violation global positivity, as discussed by Sidilkover and Roe [3].

The effect of using a non-uniform unstructured grid is investigated in Figs. 6 and 7. The unstructured grid in this case was generated using VGRID [20, 21]. The FS solution exhibits less dissipation, but is not as smooth as the FV solution. While the FS scheme preserves contact discontinuities over larger spatial ranges than the FV scheme, FS does not appear to degenerate gracefully with regard to extreme coarsening of the unstructured mesh for this test case. This behavior could have negative implications for applications employing multigrid convergence acceleration.

Circular advection. Circular advection is achieved by setting $\vec{\lambda} = (y, -x)$ and is applied on an unstructured mesh. The input profile for this case consists of both a top-hat function and a decaying sine wave, allowing comparisons between the schemes for both sharp discontinuities and smooth gradients. The input profile is

$$u(x,0) = \begin{cases} (e^{2x}\sin(2\pi x))^2 & -0.5 \le x < 0 \\ 0 & -0.6 \le x < -0.5 \\ 0.4 & -0.8 \le x < -0.6 \\ 0 & -1 \le x < -0.8 \end{cases}.$$

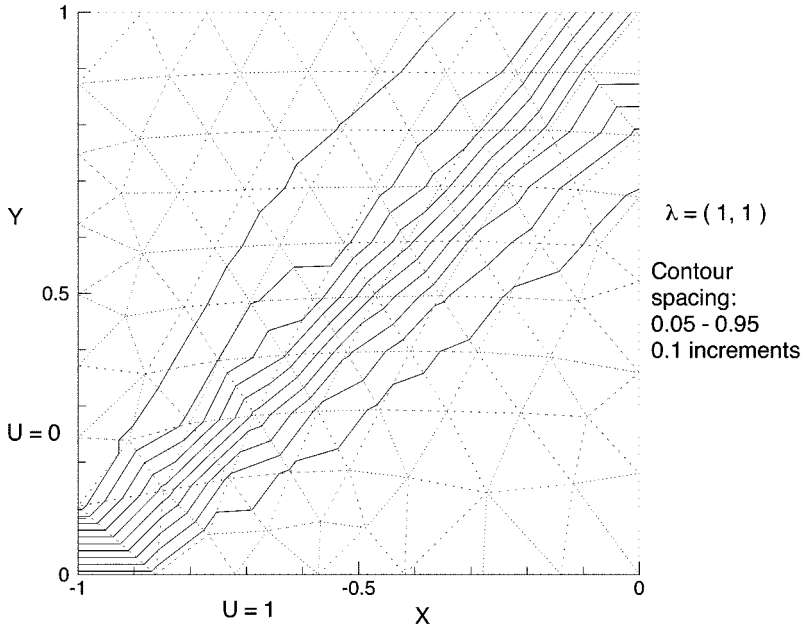

FIG. 6. Fluctuation splitting on unstructured mesh.

Results for this case are displayed in Fig. 8 for FS and Fig. 9 for FV, both using the Minmod limiter. FS performs significantly better at preserving the top-hat distribution. FS also does a better job of maintaining the minimum and maximum values of the sine distribution, though both schemes do well on the smooth gradient portion of the sine wave.

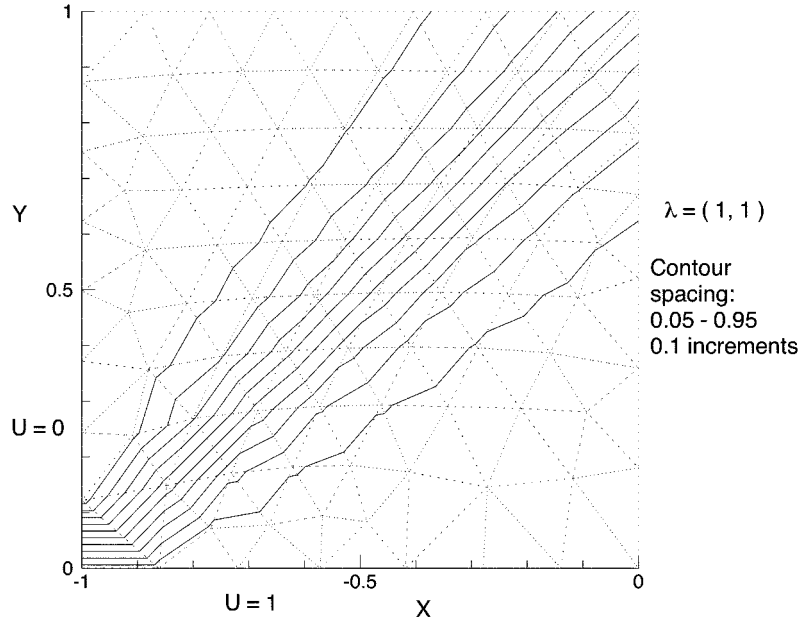

FIG. 7. Finite volume on unstructured mesh.

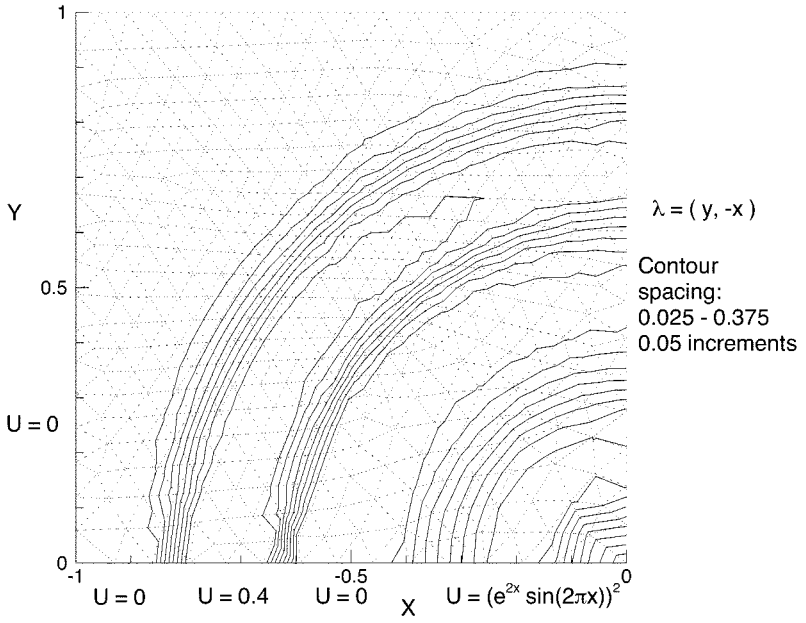

FIG. 8. Fluctuation splitting on unstructured mesh, circular advection.

Non-linear Advection

The two-dimensional inviscid Burgers equation, a non-linear advection equation, is obtained from Eq. (1) by setting $\vec{F} = (u^2/2, u)$ with $\nu = 0$. In non-conservative form the equation is written

$$u_t + uu_x + u_y = 0.$$

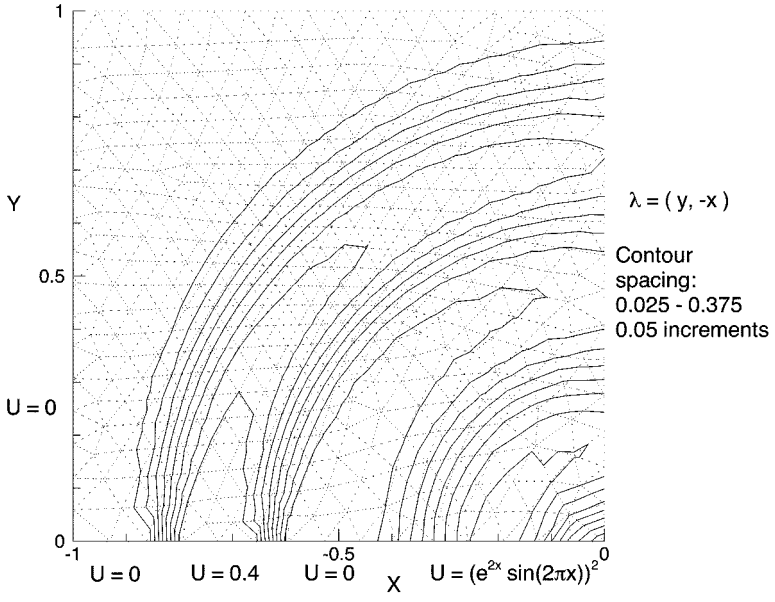

FIG. 9. Finite volume on unstructured mesh, circular advection.

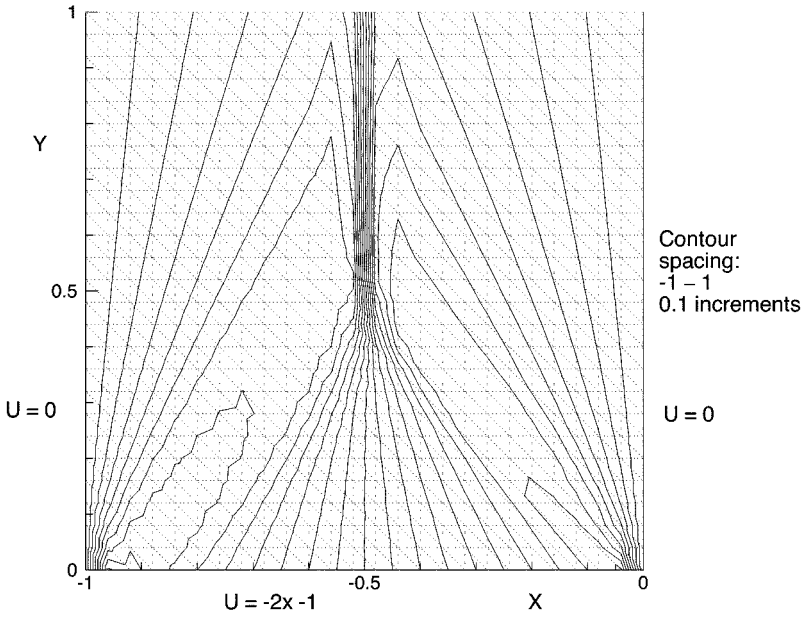

FIG. 10. Fluctuation splitting, Burgers equation.

A coalescing shock problem is considered, with an anti-symmetric input profile,

$$u(-1, y) = u(0, y) = 0$$
$$u(x, 0) = -2x - 1 \qquad \text{on } x = (-1, 0).$$

The exact solution to this problem contains symmetric expansion fans on the sides and a compression fan at the inflow that coalesces into a vertical shock at $(x, y) = (-\frac{1}{2}, \frac{1}{2})$. The fan and shock structures are features that have direct counterparts in compressible gas dynamics.

The first mesh is cut-Cartesian containing 26×26 nodes. The FS and FV solutions, both using the Minmod limiter, are presented in Figs. 10 and 11, respectively. Both algorithms exhibit the same grid dependence on the amount of artificial dissipation as seen before, with the left-half solutions having more diffusion than the right-half solutions due to the grid orientation. Both methods perform the same in the compression-fan region, coalescing into a shock to within the accuracy of the input-profile discretization. The shock is more sharply defined by FS than by FV. Figure 10 shows the correct shock speed, with nearly the entire gradient captured in one cell thickness. In contrast, Fig. 11 shows a slightly incorrect shock speed when using FV, as the shock progresses to the left beyond the coalescence point, even though the discretization is conservative. The incorrect shock speed results from a non-symmetric distribution of the dependent variable to the left and right of the shock, caused by the excessive artificial diffusion generated on the grid-misaligned (left-hand) side.

Contours of the absolute value of the error are presented in Figs. 12 and 13. Errors from both computed solutions show a lack of symmetry, again reflecting the grid dependence of the artificial diffusion terms. The error levels from FS are less than from FV. The shock curvature in the FV solution at the coalescing point is clearly visible in Fig. 13, resulting in significant downstream errors in the shock location as compared with the FS errors.

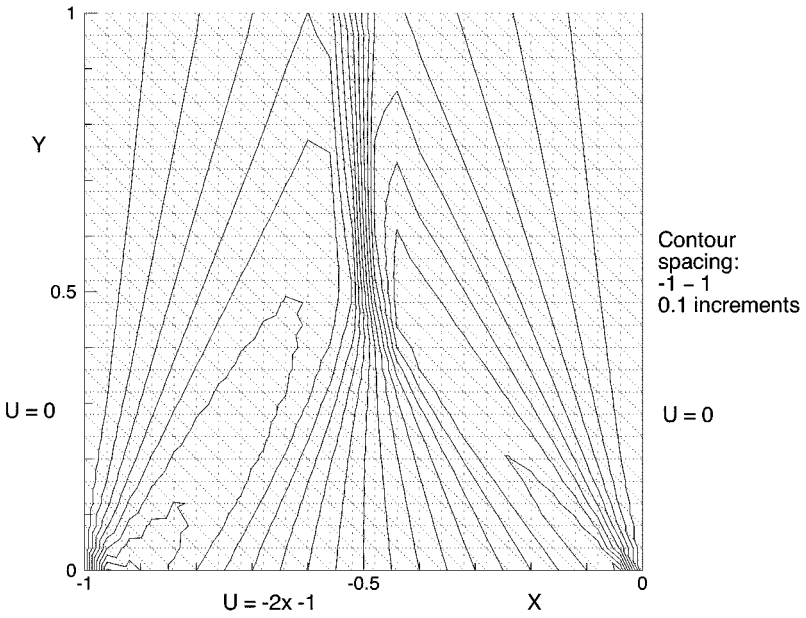

FIG. 11. Finite volume, Burgers equation.

This problem was repeated on a 25×25 mesh with symmetric diagonal cuts, favorably aligned with the advection directions (results presented in [19]). Both schemes produce the correct shock speed with symmetric error distributions on the symmetric mesh, with the same trend that FS has lower error levels than FV.

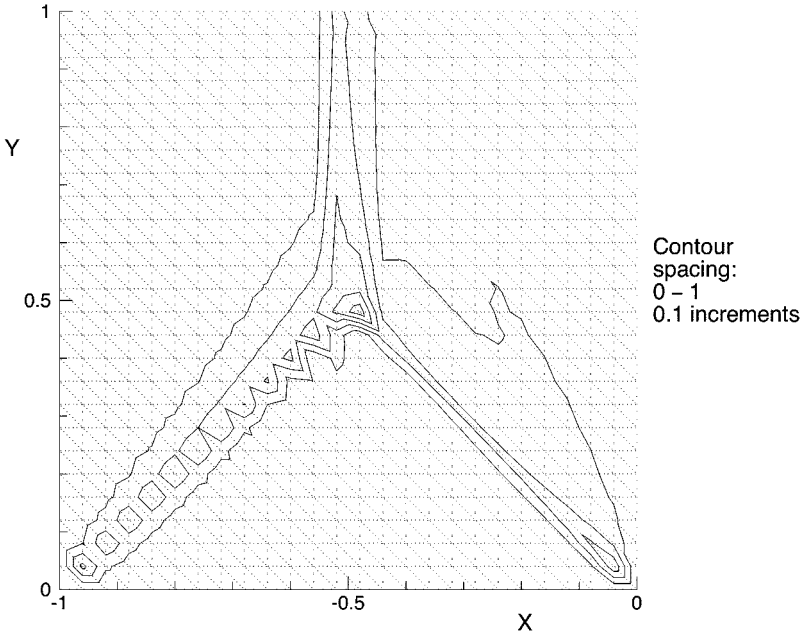

FIG. 12. Fluctuation splitting, Burgers equation, absolute error.

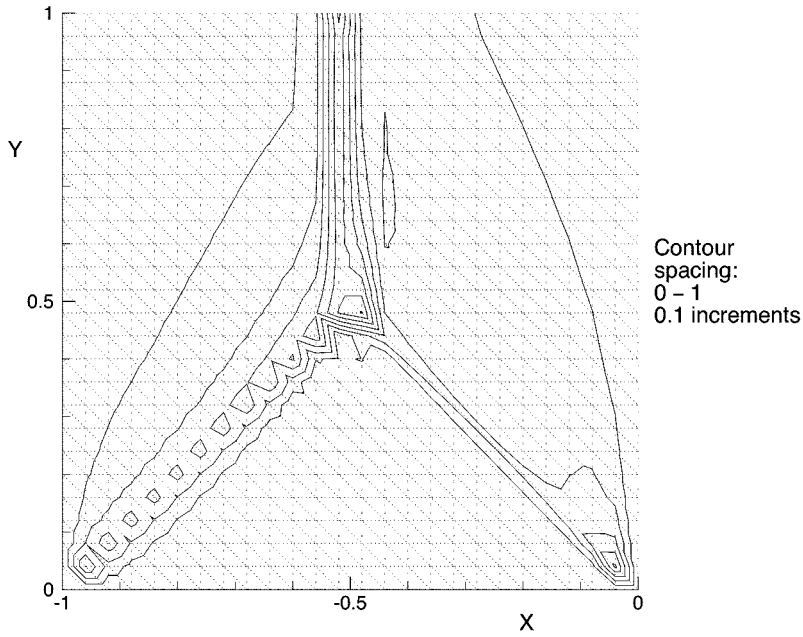

FIG. 13. Finite volume, Burgers equation, absolute error.

The final mesh for this case is a non-uniform unstructured triangulation containing 847 nodes and 1617 cells. The nodes are clustered to the outflow boundary, with a bias towards the left-hand side. The FS solution is presented in Fig. 14, showing very accurate and crisp shock resolution and good symmetry in the solution contours despite the mesh-clustering

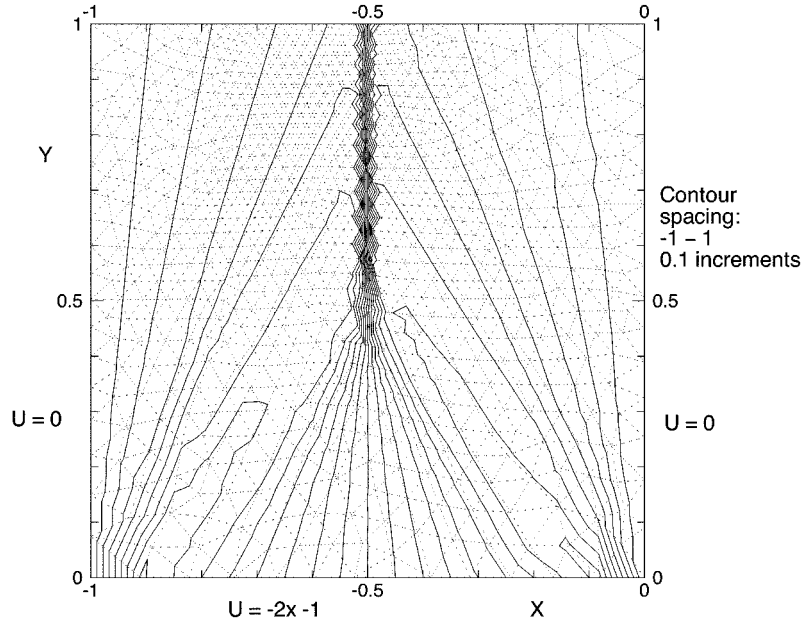

FIG. 14. Fluctuation splitting, Burgers equation, unstructured mesh.

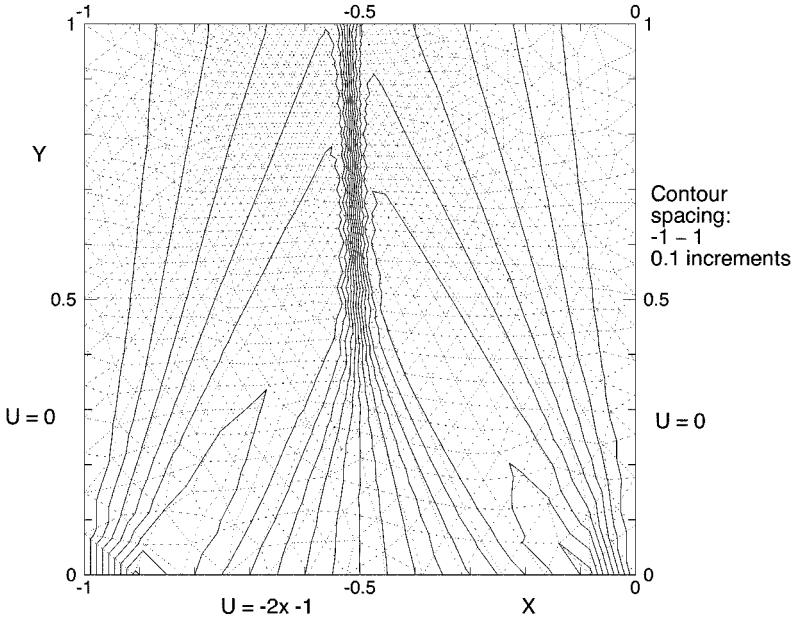

FIG. 15. Finite volume, Burgers equation, unstructured mesh.

bias. In contrast, the FV solution in Fig. 15 has a more diffuse shock and again an incorrect shock speed, with the outflow shock offset to the left of $x = -\frac{1}{2}$. In general, the FV solution is somewhat less symmetric than the FS solution.

Linear Diffusion

Choosing $\vec{F} = 0$, the diffusive heat-conduction equation is obtained from Eq. (1),

$$u_t = \nabla \cdot (\nu \nabla u).$$

The test problem, a steady-state boundary value problem on a unit square, is taken from Tomaich [4]. The Dirichlet boundary values are

$$u(-1, y) = 0, \qquad u(0, y) = \sin(\pi y) \tag{43}$$

$$u(x, 0) = 0, \qquad u(x, 1) = -\sin(\pi x). \tag{44}$$

The analytical solution on $x = [-1, 0]$, $y = [0, 1]$ is

$$u(x, y) = \frac{1}{\sinh \pi}[\sinh(\pi(x + 1)) \sin(\pi y) + \sinh(\pi y) \sin(\pi(x + 1))].$$

Both diffusion discretizations, Eqs. (10) and (28), are compared on a 438-node unstructured mesh. Figures 16 and 17 plot the absolute value of the error in the converged solutions using Eqs. (10) and (28), respectively.

The treatment of Eq. (28) is clearly more accurate for this case, and is used to discretize the diffusion terms for both FV and FS in the following section. The average-gradient results in Fig. 16 appear to exhibit a decoupling mode, similar to odd/even decoupling for structured meshes.

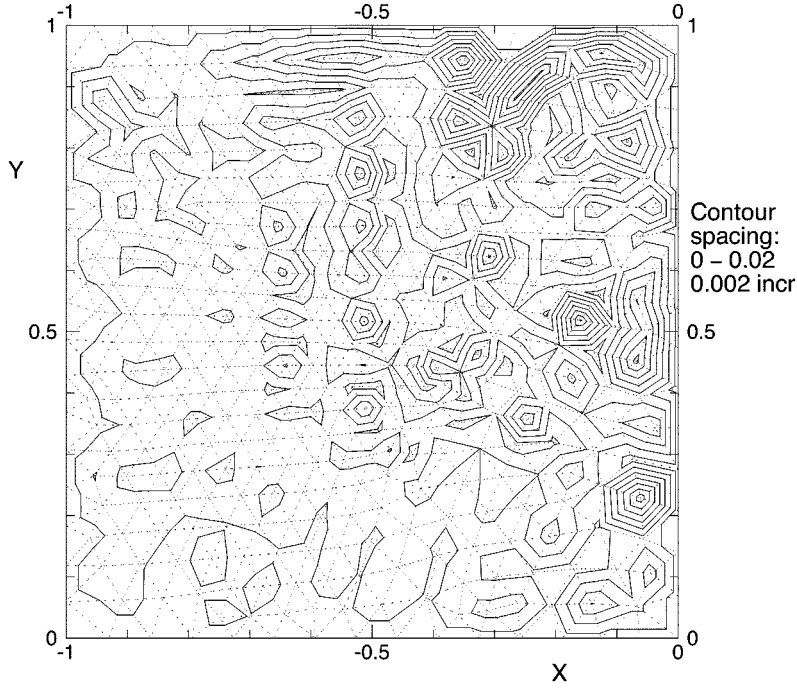

FIG. 16. Pure-diffusion problem error, diffusion terms from Eq. (10).

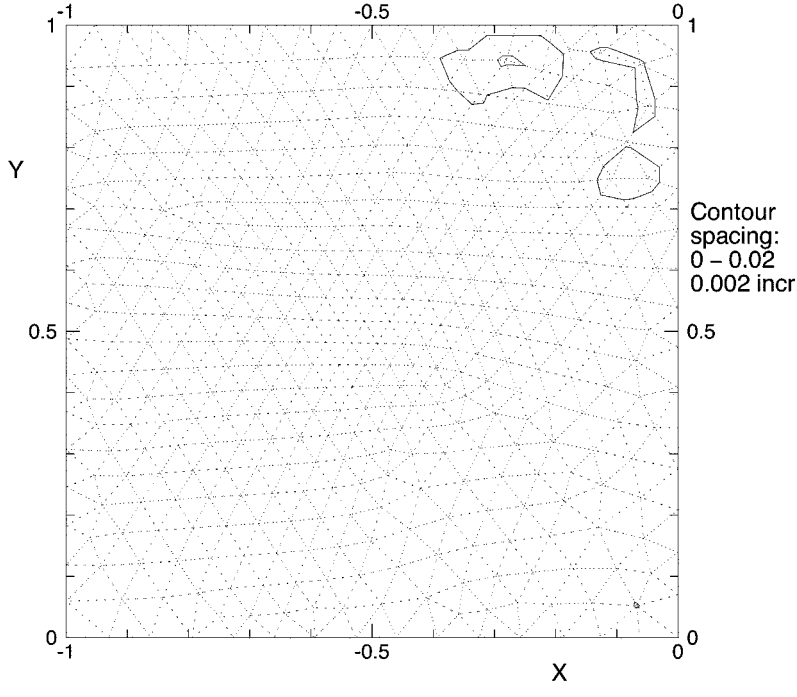

FIG. 17. Pure-diffusion problem error, diffusion terms from Eq. (28).

TABLE 1
Grids and Solution Times for Advection–Diffusion Problem

		CPU seconds	
Mesh	Nodes	FS	FV
A	134	<1	<1
B	495	1	1
C	1,928	5	8
D	7,529	64	145
E	28,915	760	1880

Linear Advection–Diffusion

The final test case is the linear advection–diffusion problem of Smith and Hutton [22]. The flux function is $\vec{F} = \vec{\lambda} u$, with

$$\vec{\lambda} = (2y(1 - x^2), -2x(1 - y^2)).$$

The streamlines for this problem, while not exactly circular, are similar in orientation to those for the circular advection problem, with the domain as a unit square in the second quadrant. The inflow profile is

$$u(x, 0) = 1 + \tanh(20x + 10).$$

The diffusion coefficient is chosen to be a constant, $\nu = 10^{-3}$. No closed-form solution is known to the authors for this problem. A small diffusion coefficient is chosen to mimic behavior that might be expected in a high-Reynolds-number shear flow. Another analogy is to the diffusion of species in multi-component gas dynamics.

A sequence of five non-uniform unstructured meshes is considered. The meshes have no preferred clustering or stretching and have nominal node-spacings of 0.1, 0.05, 0.025, 0.0125, and 0.00625, labeled as Meshes A, B, C, D, and E, respectively. The number of nodes for each mesh, along with the solution times for both FS and FV on a 195-MHz SGI R10000 CPU, are listed in Table 1.

L_2-Norms of the artificial and physical viscosities computed using both FS and FV are presented for each mesh in Table 2. Notice that the norm of the artificial dissipation for

TABLE 2
L_2-Norms ($\times 10^5$) of Artificial and Physical Viscosities for Advection–Diffusion Problem

FS			FV	
$\|\overline{\phi}\|_2$ (art.)	$\|\phi_v\|_2$ (phys.)	Mesh	$\|\Phi\|_2$ (art.)	$\|\phi_v\|_2$ (phys.)
1274	215	A	1918	190
597	265	B	640	176
192	161	C	144	119
54	76	D	46	66
13	36	E	18	36

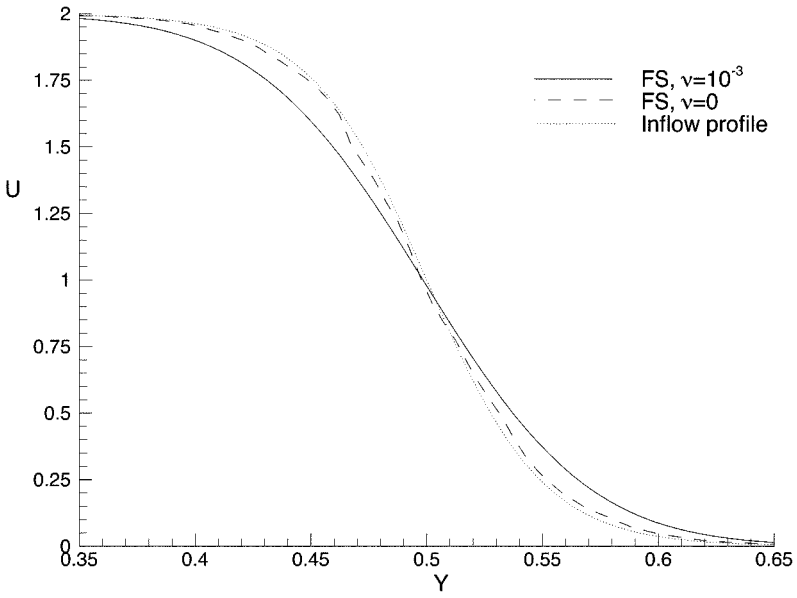

FIG. 18. Fluctuation splitting profiles on finest mesh, advection–diffusion problem.

both FV and FS is lower than the norm of the physical dissipation for Meshes D and E. Since the algorithms select only the larger of the physical or artificial dissipation (Eq. (29)), Table 2 suggests that both schemes are grid resolved by Mesh D. However, the norm of the physical dissipation is smaller for FV than FS on each mesh A–D. The physical viscosity is driven by the solution curvature, suggesting FS maintains the solution profile sharper than FV on the coarser meshes. To verify this interpretation, a comparison of outflow profiles follows.

Further evidence of a grid-resolved FS solution is seen in Figs. 18 and 19. The FS solution on Mesh E at the outflow boundary is presented along with the inflow profile and the corresponding pure-advection ($\nu = 0$) FS solution in Fig. 18. The pure-advection solution is seen to replicate the inflow profile, with a clear separation from the diffused, $\nu = 10^{-3}$, solution. Plotting only the FS results with respect to grid refinement, Fig. 19 shows grid convergence of the outflow profile by Mesh C.

The relative accuracy of FS and FV are compared in Fig. 20, where the outflow solutions from FS and FV are plotted for Meshes C and E. Taking the grid-converged FS Mesh-E solution to be the true solution, it is clear that FS reaches the grid converged solution on a coarser mesh than FV.

Computational efficiencies of the two algorithms are compared in Fig. 21, where the L_2-norm of the residual is plotted versus CPU time for the fine-mesh FS and FV solutions, along with the FS convergence history on Mesh D. The Mesh-E FS solution converges in 760 s. The corresponding FV solution takes 2.5 times longer than FS, due, in part, to the need to reconstruct gradient information at each node with FV for second-order spatial accuracy. However, considering the solution time to reach a given accuracy, it is more reasonable to compare the FS solution time on Mesh D to the finest-mesh FV solution. The FS Mesh-D solution took only 64 s, a factor of 29 times less than FV on Mesh E, and still shows better accuracy than the fine-mesh FV solution.

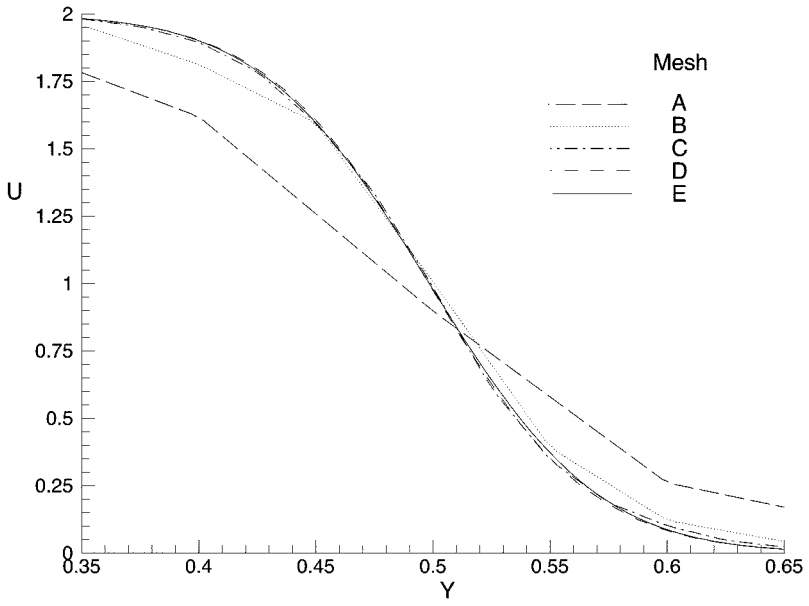

FIG. 19. Fluctuation splitting grid convergence, advection–diffusion problem.

An even greater speedup is seen with FS in conjunction with the van Albada limiter, where now the Mesh-B solution overplots the curve from the finest grid, shown in Fig. 22. The corresponding FV result using the van Albada limiter on Mesh B is included and clearly falls short of the FS accuracy. The FV case was repeated with the highly compressive Superbee limiter with little improvement in accuracy. The solution time for FS on Mesh B is about 1 s, yielding a speedup factor of 2–3 orders of magnitude over FV.

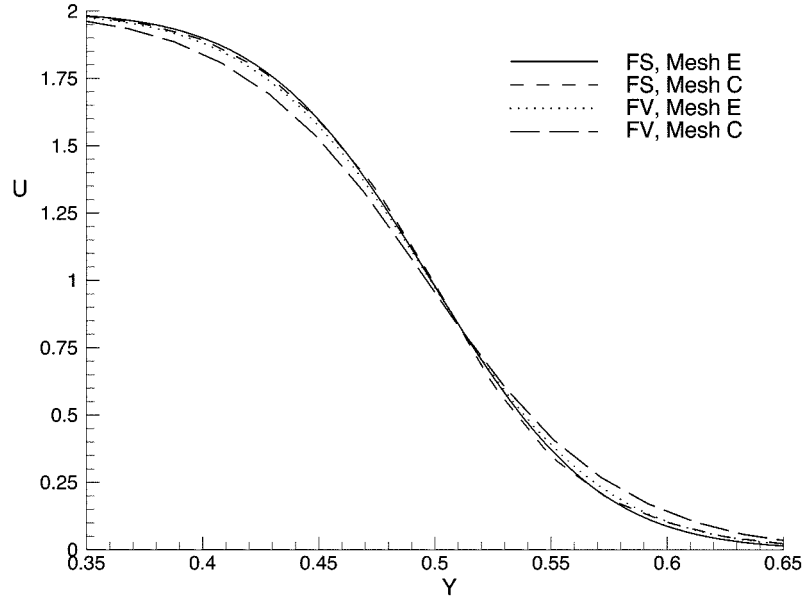

FIG. 20. Fluctuation splitting and finite volume for advection–diffusion problem.

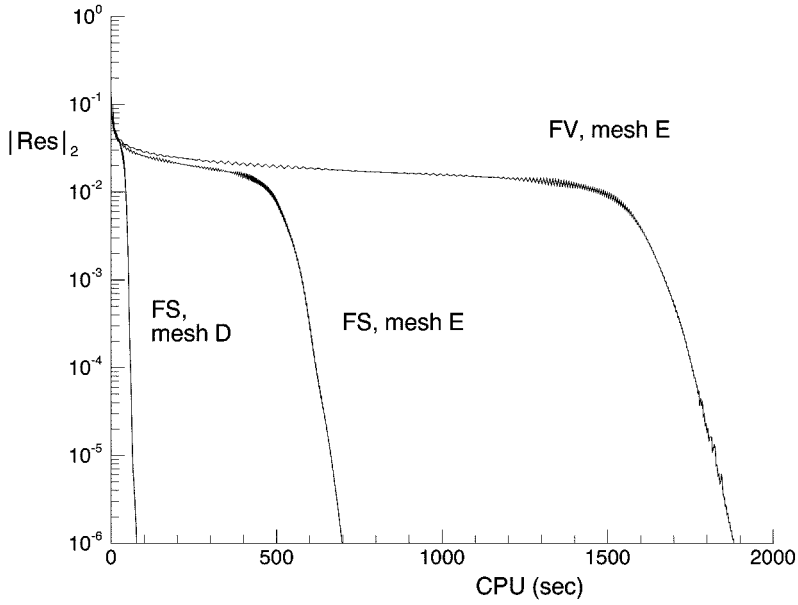

FIG. 21. Convergence histories for advection–diffusion problem.

The final set of results addresses convergence issues while pushing the positivity limits. Figure 23 compares two convergence histories for the second-order FS on Mesh B. The non-converging, though stable, convergence history is the result of using strict positivity arguments to set the timestep (Eq. (37)). The resulting solution is bounded and approximately correct but oscillatory. Limiter "ringing" is considered to be a contributor to this behavior,

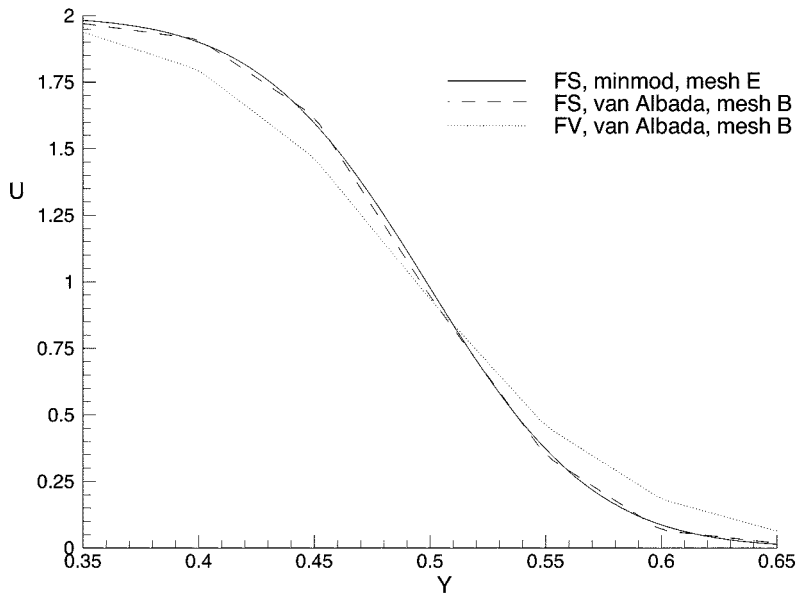

FIG. 22. Advection–diffusion results using van Albada limiter.

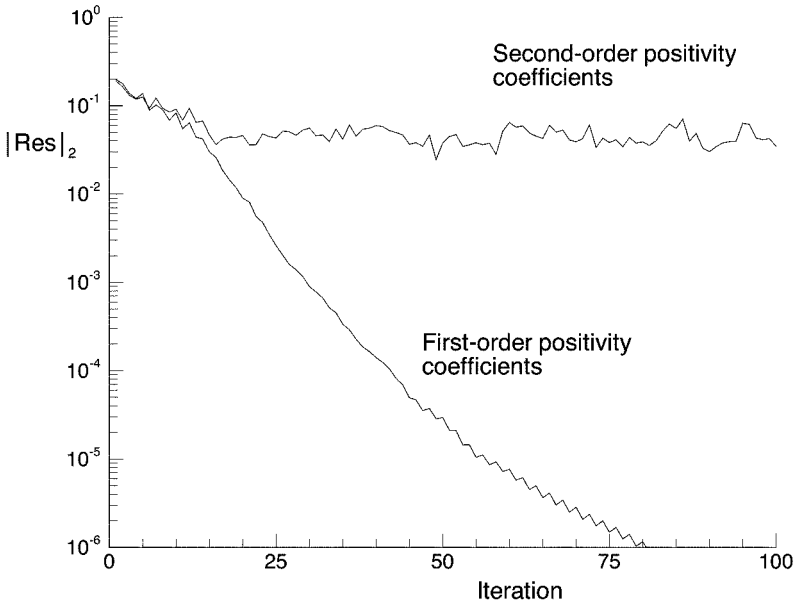

FIG. 23. Convergence rates using first- and second-order positivity coefficients.

and the higher-order discretization for the implicit matrix could be reducing the diagonal dominance, and hence stability, of the Gauss–Seidel iteration.

Full convergence is achieved by using the first-order positivity coefficients for the timestep, which are not dependent on the limiters, in conjunction with the second-order spatial discretization. The resulting local timesteps will not be as large as true second-order positivity would allow, but appear to be more robust.

SUMMARY OF RESULTS

Fluctuation splitting and finite volume schemes are compared in detail as applied to scalar advection, diffusion, and advection–diffusion problems. The specific test cases are chosen to illustrate features present in compressible gas dynamics, including expansion/compression fans and shocks for inviscid flow and high-Reynolds-number shear for viscous flows. The extensions of these schemes to systems is not covered, but is an active research area.

For the scalar equations, the fluctuation splitting scheme is seen to introduce less artificial dissipation while treating advection terms, allowing for more accurate resolution of weakly dissipative advection–diffusion problems. The ability to resolve solutions to these problems on coarser meshes makes the fluctuation splitting scheme the clear choice over finite volume.

Linear advection test problems are utilized to investigate the dependence of artificial diffusion production on grid orientation. Both fluctuation splitting and finite volume are shown to exhibit grid dependencies, but fluctuation splitting produces less artificial dissipation on all grids considered.

A non-linear coalescing shock problem further explores grid dependencies, as cases are constructed that result in incorrect shock speeds for finite volume. Fluctuation splitting shows correct shock speeds for all grids and provides tighter shock capturing than finite volume.

An advection–diffusion problem with small physical dissipation (diffusion coefficient of 10^{-3}) is considered where the reduction in artificial dissipation with fluctuation splitting results in a significant accuracy improvement over finite volume. Convergence times are compared, showing a speedup of 2.5 for fluctuation splitting over finite volume on identical grids, using a point Gauss–Seidel relaxation. However, a grid convergence study shows fluctuation splitting produces better resolution of the solution on a coarser mesh than finite volume does on a finer mesh, resulting is a speedup of 29 for fluctuation splitting over finite volume to generate a solution of comparable accuracy.

REFERENCES

1. T. J. Barth, Aspects of unstructured grids and finite-volume solvers for the Euler and Navier–Stokes equations, in *Computational Fluid Dynamics* (von Karman Institute for Fluid Dynamics, 1994), no. 1994-04 in Lecture Series.
2. L. M. Mesaros, *Multi-dimensional Fluctuation Splitting Schemes for the Euler Equations on Unstructured Grids*, Ph.D. thesis, University of Michigan (1995).
3. D. Sidilkover and P. L. Roe, *Unification of Some Advection Schemes in Two Dimensions*, Report 95-10, ICASE, Hampton (1995).
4. G. T. Tomaich, *A Genuinely Multi-dimensional Upwinding Algorithm for the Navier–Stokes Equations on Unstructured Grids Using a Compact, Highly-Parallelizable Spatial Discretization*, Ph.D. thesis, University of Michigan (1995).
5. J.-C. Carette and H. Deconinck, *Adaptive Hybrid Remeshing and SUPG/MultiD-Upwind Solver for Compressible High Reynolds Number Flows*, AIAA Paper 97-1857 (1997).
6. G. Efraimsson, A 2D analysis of the influence of artificial viscosity terms on solutions of the Euler equations, *J. Comput. Phys.* **138**, 103 (1997).
7. K.-J. Bathe, *Finite Element Procedures in Engineering Analysis* (Prentice Hall, Englewood Cliffs, NJ, 1982).
8. P. L. Roe, Approximate Riemann solvers, parameter vectors, and difference schemes, *J. Comput. Phys.* **43**, 357 (1981).
9. C. W. S. Bruner and R. W. Walters, *Parallelization of the Euler Equations on Unstructured Grids*, AIAA Paper 97-1894 (1997).
10. H. Deconinck, R. Struijs, and P. L. Roe, Fluctuation splitting for multidimensional convection problems: An alternative to finite volume and finite element methods, in *Computational Fluid Dynamics* (von Karman Institute for Fluid Dynamics, 1990), no. 1990-03 in Lecture Series.
11. H. Paillère and H. Deconinck, Compact cell vertex convection schemes on unstructured meshes, in *Euler and Navier–Stokes Solvers Using Multi-dimensional Upwind Schemes and Multigrid Acceleration*, edited by H. Deconinck and B. Koren (Vieweg, Wiesbaden, 1997), vol. 57 of *Notes on Numerical Fluid Mechanics.*
12. H. Paillère, H. Deconinck, and E. van der Weide, Upwind residual distribution methods for compressible flow: An alternative to finite volume and finite element methods. Part I. Scalar schemes, in *Computational Fluid Dynamics* (von Karman Institute, Belgium, 1997), no. 1997-02 in Lecture Series.
13. H. Deconinck, P. L. Roe, and R. Struijs, A multidimensional generalization of Roe's flux difference splitter for the Euler equations, *Comput. Fluids* **22**, 215 (1993).
14. D. Sidilkover, *A Genuinely Multidimensional Upwind Scheme and Efficient Multigrid Solver for the Compressible Euler Equations*, Report 94-84, ICASE, USA (1994).
15. G. D. van Albada, B. van Leer, and W. W. Roberts, *A Comparative Study of Computational Methods in Cosmic Gas Dynamics.* Report 81-24, ICASE, Hampton (1981).
16. C. Hirsch, *Numerical Computation of Internal and External Flows—Volume 2: Computational Methods for Inviscid and Viscous Flows* (Wiley, New York, 1990).
17. V. Venkatakrishnan, Convergence to steady state solutions of the Euler equations on unstructured grids with limiters, *J. Comput. Phys.* **118**, 120 (1995).

18. S. Spekreijse, Multigrid solution of monotone second-order discretization of hyperbolic conservation laws, *Math. Comput.* **49**, 135 (1987).
19. W. A. Wood and W. L. Kleb, *Comments on the Diffusive Behavior of Two Upwind Schemes*, NASA/TM 1998-208738 (1998).
20. S. Pirzadeh, Three-dimensional unstructured viscous grids by the advancing-layers method, *AIAA J.* **34**, 43 (1996).
21. S. Pirzadeh, *Progress toward a User-Oriented Unstructured Viscous Grid Generator*, AIAA Paper 96-0031 (1996).
22. R. M. Smith and A. G. Hutton, The numerical treatment of advection: A performance comparison of current methods, *Num. Heat Trans.* **5**, 439 (1982).